J. Plasma Phys. (2015), *vol.* 81, 905810612 © Cambridge University Press 2015
doi:10.1017/S0022377815001427

Saturation mechanism in a two-stream free-electron laser

N. Mahdizadeh†

Department of Physics, Sabzevar Branch, Islamic Azad University, Sabzevar, Iran

(Received 10 March 2015; revised 19 November 2015; accepted 23 November 2015)

The effect of a guide field on the saturation mechanism in a two-stream free-electron laser (FEL) is verified. Two monoenergetic electron beams with a vanishing pitch-angle spread are considered. Nonlinear wave–particle interaction is described by a set of coupled differential equations in a 1-D approximation. Output power is presented as a function of the axial distance. It was found that through using a focusing mechanism, the two-stream FEL reached the saturation regime in a shorter axial distance in comparison with the case of no focusing mechanism.

1. Introduction

Free-electron lasers (FELs) use a relativistic electron beam passing through a periodic transverse magnetic field to produce tunable, high power and high efficiency of coherent radiation (Sprangle, Tang & Manheimer 1980; Freund 1983; Roberson & Sprangle 1989; Freund & Antonsen 1996). By adjusting the electron beam energy and/or the wiggler parameters, the possibility of tuning the amplified frequency can be provided, making FELs very attractive devices to use. In order to improve the performance of the FELs and enhance the intensity of the parametrically excited output radiation, various configurations were proposed. In this regard, employing two electron beams rather than one has been suggested (Bekefi & Jacobs 1982). Several aspects of the two-stream FELs using kinetic and fluid approaches have been investigated (Botton & Ron 1990; Kulish, Lysenko & Savechenko 2003; Mcneil, Robb & Poole 2004; Mehdian, Saviz & Hasanbeigi 2008; Rouhani, Maraghechi & Saberi 2009; Rouhani & Maraghechi 2010; Aghamir & Mahdizadeh 2012; Mahdizadeh & Aghamir 2012).

Recently, thermal effects of slow electron beam on important quantities such as the radiation power, bunching parameter and distribution function of the pondermotive phase in two-beam FELs were studied (Mirian & Maraghechi 2013). Authors considered a linear polarized wiggler and chose the fundamental resonance of the high energy beam to attribute to the fifth harmonic of the low energy beam. In the present study, we consider a circularly polarized magnetostatic wiggler and in this situation usually the space-charge mode determines the energy difference between the two electron beams.

The use of a guide magnetic field (GMF) in the FELs is a well-known technique as a focusing mechanism (Sprangle *et al.* 1980; Freund 1983). The introduction of

† Email address for correspondence: mahdizadeh@iaus.ac.ir

https://doi.org/10.1017/S0022377815001427 Published online by Cambridge University Press

an axial GMF in the two-stream FEL configurations, especially the in Raman regime, brings about enhancement in the growth rate and other interesting effects (Liu, Yang & Liang 2006). The purpose of the present paper is to determine the nonlinear effects of the axial GMF on the saturation point, power and efficiency in two-stream FELs. Simulation has been done over a wide range of GMF strange and it was found that the introduction of an axial GMF (for example, $\hat{\Omega}_0 = 1.7$) cause the distance to saturation to decrease to approximately 37.94 %. In addition, continuous tuning of the output wavelength of the two-stream FELs can be applicable by varying the guide magnetic field intensity. In this study, two uniform, cold and relativistic electron beams with different energy and pure axial velocity were injected into the interaction region which consisted of a GMF and a helical wiggler field. A set of coupled nonlinear differential equation which describe the evolution of both electron orbits and the electrostatic and electromagnetic fields was derived and solved numerically.

In the absence of a radiation field by numerical integration of the orbit equations, the effect of the initial adiabatic increase of the wiggler field on the single-particle orbits was verified in § 2. Particle-field equations describing the nonlinear evolution of the one-dimensional two-stream FELs with a helical wiggler and an axial GMF were derived in § 3. The numerical solutions to the complete set of coupled particle-field equations have been given in § 4 and finally, § 5 is devoted to the conclusion.

2. Single particle orbit

Let us consider two monoenergetic and uniform electron beams of rest mass (m) with different energy ($\gamma_i mc^2$, γ_i is the relativistic Lorentz factor, c is speed of light in vacuum) and different density (n_{bi}) (the subscript $i = 1, 2$ refers to the different quantities of the two beams) which is injected along the positive z direction trough the circularly polarized magnetostatic field (helical wiggler) and a guide magnetic field is specifically,

$$\boldsymbol{B}(z) = B_0\hat{e}_z + B_w[\hat{e}_x \cos(k_w z) + \hat{e}_y \sin(k_w z)], \tag{2.1}$$

where B_w, B_0, $k_w = 2\pi/\lambda_w$, λ_w $\hat{e}_x$, $\hat{e}_y$, $\hat{e}_z$ are the amplitude of the wiggler field, GMF, the wiggler wave number and the wiggler period and the unit vectors of a Cartesian coordinate system, respectively.

The electron orbit equations can be obtained by substitution of the electric and magnetic fields in the Lorentz force equation, and read

$$\frac{\mathrm{d}\boldsymbol{p}_i}{\mathrm{d}t} = -e\left[\delta\boldsymbol{E} + \frac{\boldsymbol{v}_i}{c} \times (B_0\hat{e}_z + \boldsymbol{B}_w + \delta\boldsymbol{B})\right], \tag{2.2}$$

where $\delta\boldsymbol{E}$ and $\delta\boldsymbol{B}$ are the fluctuating electromagnetic fields which are easily derived from the vector and scalar potentials [2–3]. Here $\boldsymbol{p}_i$ and $\boldsymbol{v}_i$ represent the momentum and electron velocity, respectively. It is convenient to work in a rotating frame with the wiggler field defined in

$$\left.\begin{aligned}\hat{e}_1 &= \cos(k_w z)\hat{e}_x + \sin(k_w z)\hat{e}_y \\ \hat{e}_2 &= -\sin(k_w z)\hat{e}_x + \cos(k_w z)\hat{e}_y\end{aligned}\right\} \tag{2.3a}$$

$$\hat{e}_3 = \hat{e}_z. \tag{2.3b}$$

In order to examine the effect of the adiabatic increase in $B_w(z)$ on the trajectories of the electrons which enter the wiggler with purely axial motion it shall be assumed that

$$B_w(z) = \begin{cases} \frac{1}{2}B_w[1 - \cos(k_w z/4N_w)], & 0 \leqslant z \leqslant N_w\lambda_w \\ B_w, & N_w\lambda_w < z, \end{cases} \tag{2.4}$$

https://doi.org/10.1017/S0022377815001427 Published online by Cambridge University Press

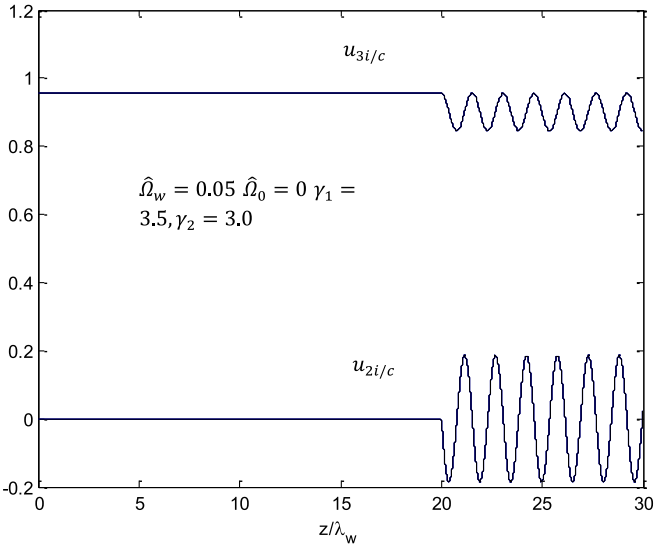


FIGURE 1. Plot of the single-particle trajectories versus axial distance for, $\hat{\Omega}_w = 0.05$, $\hat{\Omega}_0 = 0,\ \gamma_1 = 3.5,\ \gamma_2 = 3.0$.

which provides for a smooth, adiabatic transition to the constant B_w region over twenty wiggler periods. Here, N_w are the number of entry tapers of wiggler periods. The appropriate equations of motion follow from (2.2) in the absence of fluctuating fields for momentum-like variable $\boldsymbol{u}_i = \boldsymbol{p}_i/mc$ in rotating frame which were introduced in (2.3) are obtained as

$$\frac{\mathrm{d}u_{1i}}{\mathrm{d}\bar{z}} = -(\hat{\Omega}_0 - u_{3i})\frac{u_{2i}}{u_{3i}}, \tag{2.5a}$$

$$\frac{\mathrm{d}u_{2i}}{\mathrm{d}\bar{z}} = (\hat{\Omega}_0 - u_{3i})\frac{u_{1i}}{u_{3i}} - \hat{\Omega}_0, \tag{2.5b}$$

$$\frac{\mathrm{d}u_{3i}}{\mathrm{d}\bar{z}} = \hat{\Omega}_w\frac{u_{2i}}{u_{3i}}, \tag{2.5c}$$

where, $\hat{\Omega}_w = (eB_w)/(mc^2k_w)$ is a function of the axial position (z) and $\hat{\Omega}_0 = (eB_0)/(mc^2k_w)$ is scaled GMF. As an example, we consider energy of the beams which corresponding to $\gamma_1 = 3.5$, $\gamma_2 = 3.0$ and a wiggler field in which $\hat{\Omega}_w = 0.05$. We plot u_{3i} and u_{2i} versus axial position that is seen in figure 1. The electron trajectory exhibits small oscillations about the steady-state orbit. The value of u_{2i} remain small ($u_{2i} \cong 0$) over the entire course of the trajectory. Plot of u_{3i} also exhibit a small oscillation about the value for the steady-state orbit; however mean value of it is less than its initial value.

As magnitude of the $\hat{\Omega}_0$ (corresponding to an increase in GMF) increases from 0 to 0.62 the magnitude of the fluctuation relative to the steady-state bulk value u_{2i} increases, this fact is shown in figure 2. Increases in u_{2i} cause an increase in the interaction time of the particles with the wave and as a result it [increases in fluctuation of u_{2i}] causes to reach the shorter distance to saturation, which will be discussed in the next sections.

https://doi.org/10.1017/S0022377815001427 Published online by Cambridge University Press

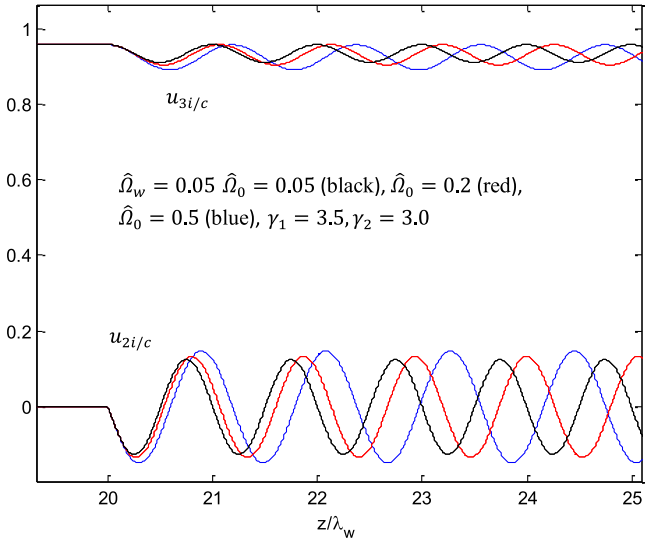


FIGURE 2. Plot of the single-particle trajectories versus axial distance for $\hat{\Omega}_w = 0.05$, $\hat{\Omega}_0 = 0$ (black), $\hat{\Omega}_0 = 0.2$ (red), $\hat{\Omega}_0 = 0.5$ (blue), $\gamma_1 = 3.5$, $\gamma_2 = 3.0$.

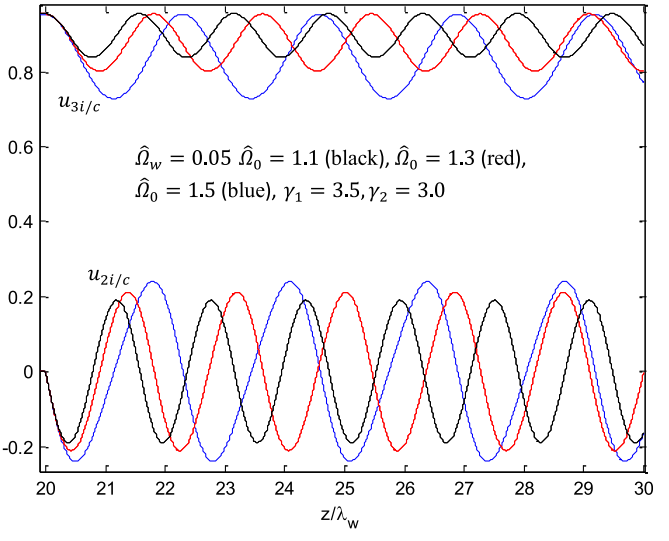


FIGURE 3. Plot of the single-particle trajectories versus axial distance for $\hat{\Omega}_w = 0.05$, $\hat{\Omega}_0 = 1.1$ (black), $\hat{\Omega}_0 = 1.3$ (red), $\hat{\Omega}_0 = 1.5$ (blue), $\gamma_1 = 3.5$, $\gamma_2 = 3.0$.

Parameters consistent with Group-II steady-state orbits are considered in figure 3. With an adiabatic rise in wiggler magnitude, we encounter an increase in the magnitude of u_{2i}, however, small oscillations about mean values are found in constant wiggler amplitude region. In this regime, perturbation about the steady-state orbits is large. Although increasing the strange of the GMF along with the steady-state axial velocity, it causes to decrease the perturbations about the helical orbits, as is shown in figure 3.

https://doi.org/10.1017/S0022377815001427 Published online by Cambridge University Press

As the GMF strange is increased, perturbation about the steady-state orbits increases. In the special range of the GMF strange, (i.e. $1.788 \leqslant \hat{\Omega}_0$) for $\hat{\Omega}_w = 0.05$, $\gamma_1 = 3.5$ and $\gamma_2 = 3.0$ large fluctuations in the electron velocity occur. However, for $\hat{\Omega}_0 \leqslant 1.788$, transverse components of the electron velocity may become small which the radial excursions of the electron beam make it easy for the beams to propagate.

3. Particle-field equations

In order to derive the dynamical equations which govern the evolution of the radiation the scalar and vector potentials of radiation and space-charge wave are substituted into the Maxwell's equations. The vector potential of the radiation field can be written as

$$\delta \boldsymbol{A}(z, t) = \delta \hat{A}(z)[\hat{e}_x \cos \alpha_+(z, t) - \hat{e}_y \cos \alpha_+(z, t)] \tag{3.1}$$

and

$$\delta \emptyset(z, t) = \delta \widehat{\emptyset}(z) \cos \alpha(z, t), \tag{3.2}$$

where $\delta \hat{A}(z)$ and $\delta \widehat{\emptyset}(z)$ are the time-independent amplitudes of vector and scalar potentials. The phase of an electromagnetic wave of frequency ω and wavenumber k_+ is given by

$$\alpha_+(z, t) = \int_0^z \mathrm{d}\acute{z}\, k_+(\acute{z}) - \omega t \tag{3.3}$$

and

$$\alpha(z, t) = \int_0^z \mathrm{d}\acute{z}\, k(\acute{z}) - \omega t \tag{3.4}$$

is the phase of the space-charge wave with the same frequency but wavenumber k. By substituting microscopic fields and source current in Maxwell's equations and assuming slowly varying amplitudes and wavenumbers over a wavelength (slow time-scale approximation) one could obtain the field equations (Freund & Antonsen 1996; Raghavi, De Ninno & Mehdian 2008; Mahdizadeh & Aghamir 2012). The procedure is similar to (Freund & Antonsen 1996; Raghavi *et al.* 2008) and results are given in the following equations,

$$\frac{\mathrm{d}\delta a}{\mathrm{d}\bar{z}} \equiv \Gamma_+ \delta a, \tag{3.5a}$$

$$\frac{\mathrm{d}\Gamma_+}{\mathrm{d}\bar{z}} = (-\bar{\omega}^2 + \bar{k}_+^2 - \Gamma_+^2) + \sum_{i=1}^{2} \frac{\omega_{bi}^2}{\delta a} \left\langle \frac{u_{1i} \cos \psi_i - u_{2i} \sin \psi_i}{|u_{3i}|} \right\rangle, \tag{3.5b}$$

$$\frac{\mathrm{d}\bar{k}_+}{\mathrm{d}\bar{z}} = -2\bar{k}_+ \Gamma_+ - \sum_{i=1}^{2} \frac{\omega_{bi}^2 \beta_{z0i}}{\delta a} \left\langle \frac{u_{1i} \sin \psi_i - u_{2i} \cos \psi_i}{|u_{3i}|} \right\rangle, \tag{3.5c}$$

$$\frac{\mathrm{d}\delta\varphi}{\mathrm{d}\bar{z}} = -2 \sum_{i=1}^{2} \frac{\omega_{bi}^2 \beta_{z0i}}{\bar{\omega}} \langle \sin \psi_{sci} \rangle, \tag{3.5d}$$

where, Γ_+ defines the growth rate (i.e. the logarithmic derivative) of the vector potential, $\delta a = (e\delta \hat{A}(\bar{z}))/mc^2$, $\delta\varphi = (e\delta \widehat{\emptyset}(\bar{z}))/mc^2$, $\omega_{bi}^2 = (4\pi n_i e^2)/mc^2$ are the scaled amplitude of the vector potential, scaled amplitude of the space-charge potential and the plasma frequency denoted by the ambient beam density, respectively. Here,

https://doi.org/10.1017/S0022377815001427 Published online by Cambridge University Press

$\psi \equiv \alpha_+(\bar{z}, \bar{t}) + \bar{z}$ and $\psi_{sc}(\equiv \alpha(\bar{z}, \bar{t}))$ are the ponderomotive and space-charge phases, respectively, which are given as

$$\frac{\mathrm{d}\psi_i(\bar{z})}{\mathrm{d}\bar{z}} = \bar{k}_+(\bar{z}) + 1 - \frac{\bar{\omega}}{\beta_{3i}}, \tag{3.6a}$$

$$\frac{\mathrm{d}\psi_{sci}(\bar{z})}{\mathrm{d}\bar{z}} = \bar{k}(\bar{z}) - \frac{\bar{\omega}}{\beta_{3i}}. \tag{3.6b}$$

In the above differential equations, we have changed the integration parameter from $\bar{t}$ to $\bar{z}$, according to the relation $\mathrm{d}/\mathrm{d}\bar{t} = \beta_3(\mathrm{d}/\mathrm{d}\bar{z})$ (which $\beta_{3i} = v_{3i}/c$). It is convenient to scale all quantities to c (speed of light in vacuum) and k_w, i.e. $\bar{t} = tck_w$, $\bar{z} = zk_w$, $\bar{\omega} = \omega/ck_w$, $\bar{k} = k/k_w$, $\bar{t}_0 = t_0 ck_w$, $\bar{\omega}_{bi} = \omega_{bi}/ck_w$.

The averaging operator $\langle(\cdots)\rangle = (1/2\pi)\int_{-\pi}^{\pi} \sigma(\psi_0)\,\mathrm{d}\psi_0(\cdots)$ is defined over an ensemble of beam electrons injected into the interaction region within one wave period. Here, $\sigma(\psi_0)$ refers to the initial beam distribution in phase. Since it is assumed that the beams are uniformly distributed, it is taken as $\sigma(\psi_0) = 1$ where $\psi_0(= -\bar{\omega}\bar{t}_0)$ is the initial phase, and $\bar{t}_0$ is scaled injection time. Derivation of dynamical equations (3.5*a–d*) is presented in the appendix A.

Since we treat the case of a steady-state amplifier configuration, one may integrate z and write the Lorentz force equations as (Freund & Antonsen 1996)

$$\frac{\mathrm{d}u_{1i}}{\mathrm{d}\bar{z}} = -(\hat{\Omega}_0 - u_{3i})\frac{u_{2i}}{u_{3i}} + \left[\delta a\left(\frac{\omega}{v_{3i}} - \bar{k}_+\right)\sin\psi_i + \frac{\mathrm{d}\delta a}{\mathrm{d}\bar{z}}\cos\psi_i\right], \tag{3.7a}$$

$$\frac{\mathrm{d}u_{2i}}{\mathrm{d}\bar{z}} = (\hat{\Omega}_0 - u_{3i})\frac{u_{1i}}{u_{3i}} + \left[\delta a\left(\frac{\omega}{v_{3i}} - \bar{k}_+\right)\cos\psi_i - \frac{\mathrm{d}\delta a}{\mathrm{d}\bar{z}}\sin\psi_i\right] - \hat{\Omega}_w, \tag{3.7b}$$

$$\begin{aligned}\frac{\mathrm{d}u_{3i}}{\mathrm{d}\bar{z}} &= \bar{k}_+\delta a\frac{u_{1i}\sin\psi_i + u_{2i}\cos\psi_i}{u_{3i}} - \frac{1}{\beta_{3i}}\left(\bar{k}\delta\varphi_i\sin\psi_{sci} - \frac{\mathrm{d}}{\mathrm{d}\bar{z}}\delta\varphi_i\cos\psi_{sci}\right)\\ &\quad + \hat{\Omega}_w\frac{u_{2i}}{u_{3i}} - \frac{\mathrm{d}\delta a}{\mathrm{d}\bar{z}}\frac{u_{1i}\cos\psi_i - u_{2i}\sin\psi_i}{u_{3i}}.\end{aligned} \tag{3.7c}$$

It has been assumed that the amplitudes and phases are slowly varying functions of position, i.e. $|\partial\delta a/\partial z| \ll |k_+\delta a|$, and this occurs only in a vicinity of the wave-particle resonance at $\omega \approx (k_+ + k_w)v_{3i}$.

Equations (3.5) and (3.6) together with (3.7) give a set of $10N + 4$ self-consistent first order nonlinear differential equations which describe the wave evolution in the two-stream FEL. Here N refers to the total number of electrons, subjected to the initial conditions.

4. Numerical solutions

Using the fourth-order Runge–Kutta method, the set of coupled differential equations (3.5)–(3.7), has been solved numerically for a two-stream FEL working in amplifier mode. A wave (ω, k_+) of arbitrary amplitude is injected into the system in concert with two relativistic, monoenergetic and noiseless electron beams. The typical parameters of the two-stream FEL system used in this work are the same with the numerical analyses which have been listed in table 1.

The averages in the dynamical equations have been calculated by the Simpson's rule in each of the variables with a total 17 semi-particles per wave period. The

https://doi.org/10.1017/S0022377815001427 Published online by Cambridge University Press

Different quantities	Value
Maximum magnetic field (B_w)	2.142 kG
Length of the wiggler period (λ_w)	2 cm
Initial radius of beam	0.155 cm
Average beam energy (E)	0.135 MeV
ΔE (the energy difference between two beams)	0.025 MeV
Range of the scaled GMF	0–2.2
N_w (scaled entry taper region)	20

TABLE 1. Two-stream FEL parameters under consideration.

electrons are uniformly distributed in phase for $-\pi \leqslant \psi_0 \leqslant \pi$ in order to model the case of a continual and un pre-bunched beam. The wiggler field is assumed to increase adiabatically to a constant level over twenty wiggler periods. Since the wiggler field increases adiabatically from zero at the entry plane, the growth rate of the vector potential is initially zero as well (i.e. $(\Gamma_+)_0 = 0$). The electromagnetic mode was chosen to correspond to the wave characterized by the highest linear growth rates. For a finite value of initial scalar potential and a uniform initial electron distribution the initial $\bar{k}$ value vanishes. The arbitrary initial values for the vector and scalar potentials are the same and they are of order 1.0×10^{-6}. Generally, the frequency of the amplified wave is determined by the intersection of the slow space-charge wave mode and the transverse electromagnetic mode.

Corresponding, the initial value of the axial velocity may be obtained by solving a cubic equation, which results from requiring the conservation of the total energy for the steady state orbits. Substituting γ_{0i}, ω and v_{0zi} into the transverse electromagnetic mode one can obtain the initial value of the k_+.

An example of the simulation results for the Group I orbit is shown in figure 4 in which the radiation field amplitude which is corresponding to the power is plotted as a function of axial position for the case in which $\hat{\Omega}_w = 0.4$, $\gamma_1 = 3.5$, $\gamma_2 = 3.0$, $\bar{\omega}_{b1} = 0.4$, $\bar{\omega}_{b2} = 0.42$, for some different value of the axial GMF such as: $\hat{\Omega}_0 = 0.05$ (red), $\hat{\Omega}_0 = 0.1$ (green) and $\hat{\Omega}_0 = 0.2$ (blue), $\hat{\Omega}_0 = 0.4$ (black, thin), $\hat{\Omega}_0 = 0.5$ (cyan) and without a GMF (black, thick: ■). It is explicitly seen from the figure that, using GMF leads to an elevated increase in the amplitude and further decline in the distance to saturation. The input signal frequency depends on the axial GMF as well as the other initial two-stream FELs parameter. In the case of no GMF for $0 < z/\lambda_w \leqslant 8.721$, the amplitude which corresponds to the power remains almost at its initial value ($\cong 10^{-6}$), such region corresponds to the small signal regime. Amplitude increases exponentially for $8.721 \leqslant z/\lambda_w$ and continues the increase up to $z/\lambda_w \cong 70.37$, which is the saturation point but the radiation amplitude does not increase. The region where amplitude increase exponentially i.e. $8.721 \leqslant z/\lambda_w < 70.37$ is the nonlinear regime and $z/\lambda_w = 70.37$ is the saturation point with scaled amplitude of $\delta a \cong 0.02005$ (for the case of $\hat{\Omega}_0 = 0$).

Different values of saturation point stemmed from different GMF strengths, as seen in figures 5 and 6. For instance, in the case of $\hat{\Omega}_0 = 0.5$ (cyan), the amplitude of the radiation begins to be amplified at $z/\lambda_w = 2.51$ and the saturation point is at $z/\lambda_w = 31.33$ with scaled amplitude of $\delta a \cong 2.29$. This range of GMF corresponds to Group I single particle trajectories with $v_{0z1}/c = 0.9715$, $v_{0z2}/c = 0.9434$ and in this range the resonant frequency as well as the efficiency are lower.

https://doi.org/10.1017/S0022377815001427 Published online by Cambridge University Press

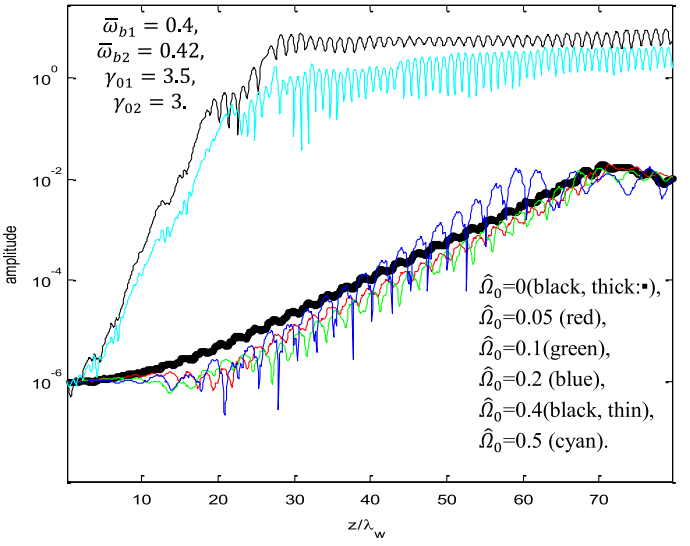


FIGURE 4. Graphs of the amplitude of the radiation field versus axial coordinate for: $\hat{\Omega}_0 = 0$ (black, thick: ■), $\hat{\Omega}_0 = 0.05$ (red), $\hat{\Omega}_0 = 0.1$ (green), $\hat{\Omega}_0 = 0.2$ (blue), $\hat{\Omega}_0 = 0.4$ (black, thin), $\hat{\Omega}_0 = 0.5$ (cyan).

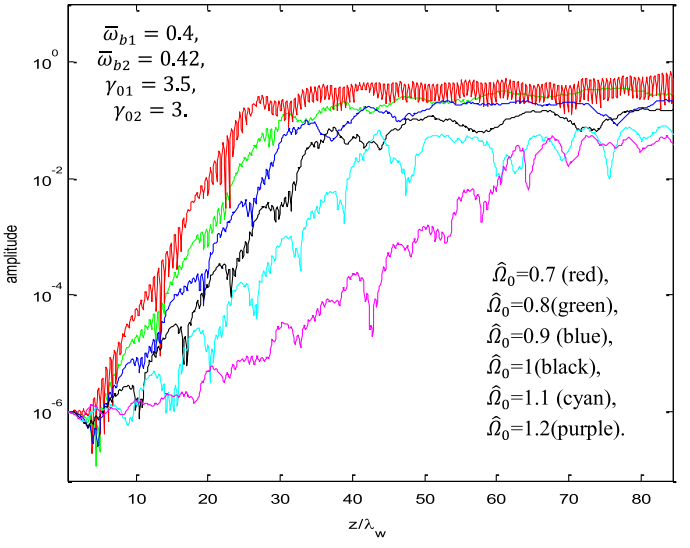


FIGURE 5. Graphs of the amplitude of the radiation field versus axial coordinate for: $\hat{\Omega}_0 = 0.7$ (red), $\hat{\Omega}_0 = 0.8$ (green), $\hat{\Omega}_0 = 0.9$ (blue), $\hat{\Omega}_0 = 1$ (black), $\hat{\Omega}_0 = 1.1$ (cyan), $\hat{\Omega}_0 = 1.2$ (purple).

Increases in the axial GMF lead to a longer distance to saturation above the value $\hat{\Omega}_0 = 0.5$ up to $\hat{\Omega}_0 = 1.4$ as shown in figures 4 and 5. It is worth mentioning that in order to compare the saturation distance, efficiency and single particle orbit in case there is GMF or not, all quantities for the two cases are the same i.e. total

https://doi.org/10.1017/S0022377815001427 Published online by Cambridge University Press

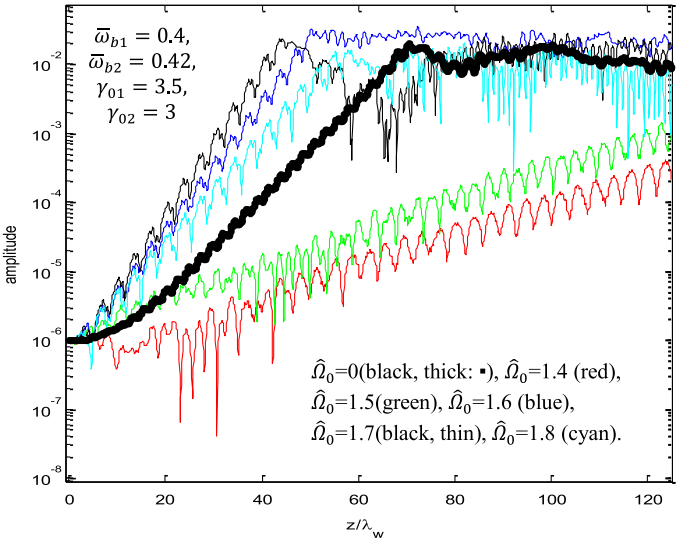


FIGURE 6. Graphs of the amplitude of the radiation field versus axial coordinate for: $\hat{\Omega}_0 = 0$ (black,thick: ■), $\hat{\Omega}_0 = 1.4$ (red), $\hat{\Omega}_0 = 1.5$ (green), $\hat{\Omega}_0 = 1.6$ (blue), $\hat{\Omega}_0 = 1.7$ (black, thin), $\hat{\Omega}_0 = 1.8$ (cyan).

current, initial energy of the electrons and so on. To compare the effect of GMF on the distance to saturation and wave amplitude it is evident from figure 6 in which in the case of $\hat{\Omega}_0 = 1.7$ (black, thin), scaled distance to saturation is 43.67 (87.34 cm); however, in the case of no GMF it is 70.37 (140.74 cm). At the same time, scaled wave amplitude in the case of $\hat{\Omega}_0 = 1.7$ (black, thin) is 0.02399, however in the latter case is 0.02005 and scaled resonant frequency for two cases of $\hat{\Omega}_0 = 1.7$ (black, thin) and $\hat{\Omega}_0 = 0$ (black, thick) is the same and it is 5.837. The distance to saturation decrease to about 37.94 % because of the presence of the axial GMF; however, the decrease in the saturation length employing the ion-channel guide in FEL is about 30 % (Raghavi *et al.* 2008). But, the wave amplitude does not have a considerable increase within both output enhancement (i.e. the ion-channel and axial GMF). The beating of the wiggler and the electromagnetic wave result in the ponderomotive potential and when the bunched electrons trapped in that's potential saturation occurs, upsurges in the GMF cause (1) to increase the fluctuation levels in the electron velocities about the steady-state trajectories, (2) decrease axial component of velocities, alternatively, increase quiver velocity (3) decline divergence of the electron beam and these effects will compete with the increases in the efficiency and power. A summary of the distance to saturation and maximum amplitude of radiation are shown in figure 7 as functions of scaled GMF.

It is evident from figure 7 that shorter distance to saturation occur for $\hat{\Omega}_0 = 0.5$. Initially distance to saturation decreases for values $\hat{\Omega}_0 < 0.5$ then increases (for the range of $0.5 < \hat{\Omega}_0 < 1.4$), after that decreases (for the range of $1.4 < \hat{\Omega}_0 < 1.7$) and finally increases. Using the GMF cause to increases maximum amplitude of radiation. The larger amplitude occurs for the scaled GMF strange of $\hat{\Omega}_0 = 0.4$. More increases in GMF strength decrease the maximum amplitude of radiation as shown in figure 7.

https://doi.org/10.1017/S0022377815001427 Published online by Cambridge University Press

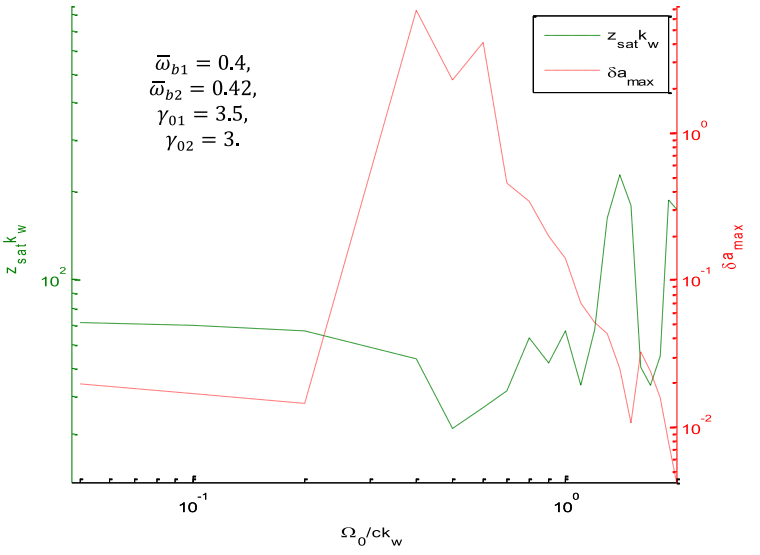


FIGURE 7. Graphs of the distance to saturation (dashed line) and the maximum amplitude (dotted line) versus scaled GMF strength.

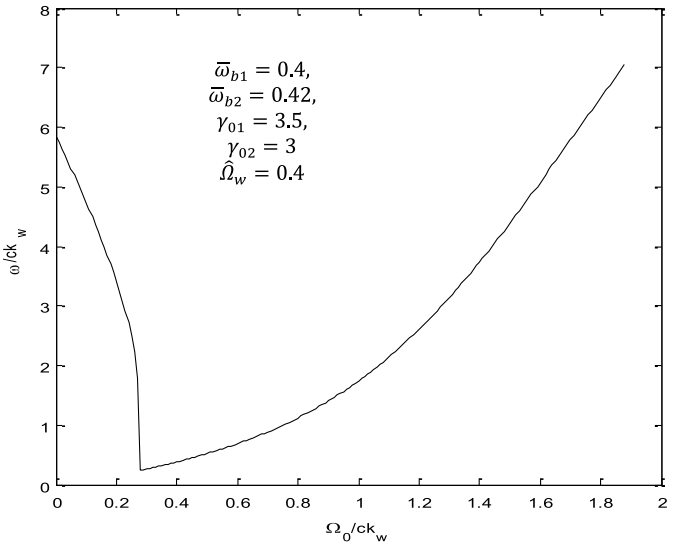


FIGURE 8. Graphs of the resonant frequency versus axial GMF strange for $\hat{\Omega}_w = 0.4$, $\bar{\omega}_{b1} = 0.4$, $\bar{\omega}_{b2} = 0.42$, $\gamma_{01} = 3.5$, $\gamma_{02} = 3$.

The resonant frequency versus axial GMF strange for a typical value of wiggler strange ($\hat{\Omega}_w = 0.4$) was shown in figure 8. First resonant frequency decreases and then for the range of $\hat{\Omega}_0 > 0.287$ it increases. By adjusting the axial GMF strange, tuning a given wiggler configuration at different output wavelength is applicable. For a benchmark in our study, when we consider all quantities of each beam equal to zero results of Freund & Antonsen (1996), Raghavi *et al.* (2008) are recovered.

https://doi.org/10.1017/S0022377815001427 Published online by Cambridge University Press

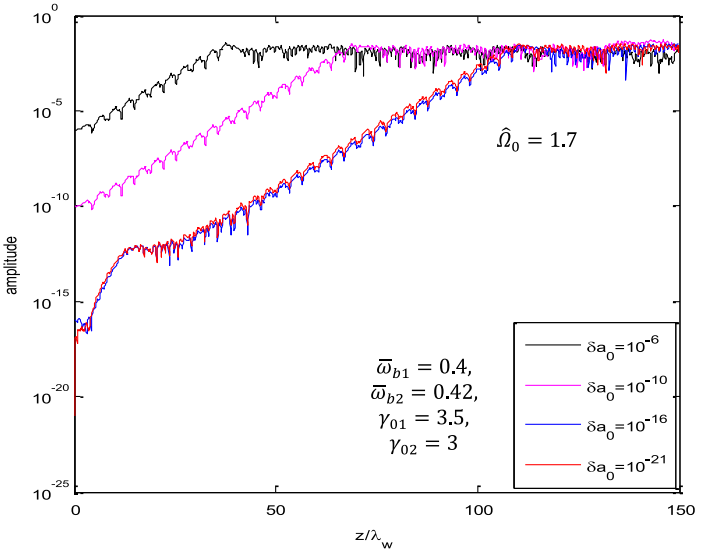


FIGURE 9. Graphs of the amplitude of the radiation field versus axial coordinate for different value of the seed intensity.

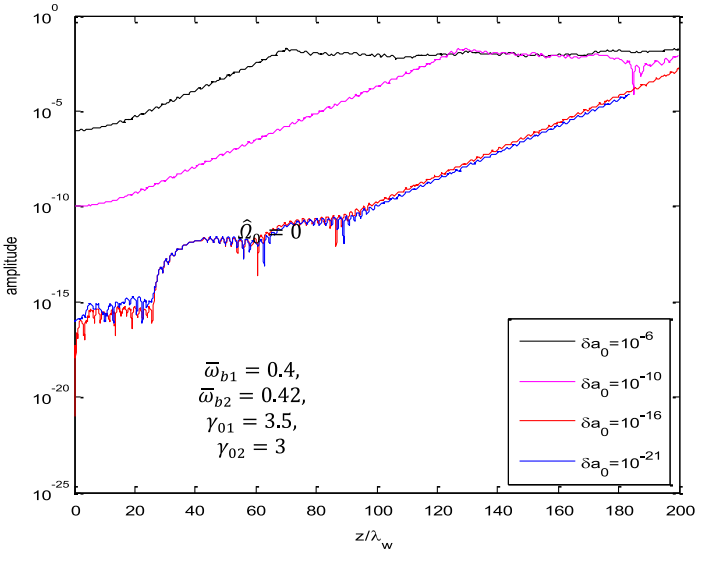


FIGURE 10. Graphs of the amplitude of the radiation field versus axial coordinate for different value of the seed intensity.

Maximum wave amplitude of the output radiation does not depends on the initial amplitude of the seed. However, for the seeds with the least initial amplitude, ratio of the final electromagnetic (EM) wave amplitude to the initial amplitude have maximum value, as shown in figures 9 and 10. It is evident from the figures that the seeds with high intensity decreases the distance to saturation because the seeds with high intensity hastens bunching process of the electron and result particle trapping in the ponderomotive potential. The efficiency can be defined as the ratio of the output

https://doi.org/10.1017/S0022377815001427 Published online by Cambridge University Press

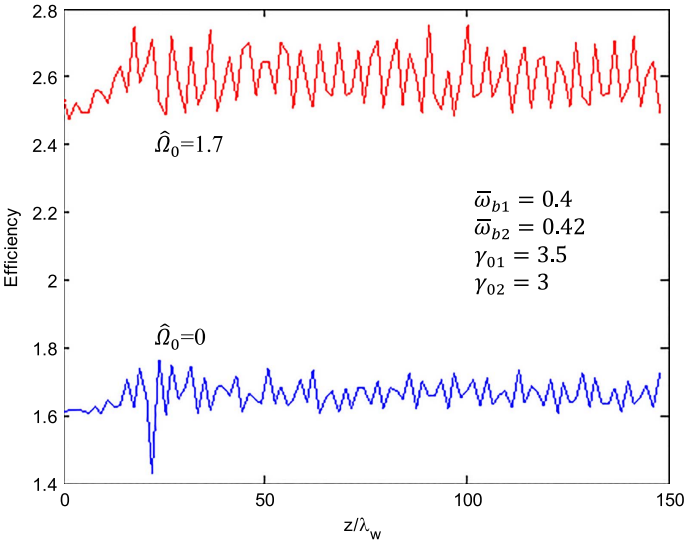


FIGURE 11. Graphs of the efficiency versus scaled longitudinal distance for: $\hat{\Omega}_0 = 0$ (blue), $\hat{\Omega}_0 = 1.7$ (red).

radiation field energy-flux increase to the initial beams-energy-flux and it is given by

$$\eta \cong \frac{ck\omega}{\sum_{i=1}^{2} \omega_{bi}^2(\gamma_i - 1)\beta_{zi}}(\delta a_{sat})^2, \tag{4.1}$$

where the η shows net energy transfers to the wave and δa_{sat} is the radiation field amplitude at saturation.

The axial position dependence of the linear efficiency is illustrated in figure 11 for two cases with and without considering the GMF. It is clear from the figure that efficiency increases while we consider the GMF. In the case of no GMF it is about mean value 1.65 %. However, when we consider GMF it is about 2.61 %. in this case, the evolution of radiation fields become more regular as well.

Maximum amplitude and the distance to saturation as a function of scaled the difference of initial two beams energy are plotted in figure 12. It is evident from the figure that for the value of $\Delta\gamma = 0.9$ the amplitude of the radiation has maximum value; however, for the range of $0.45 \leqslant \Delta\gamma \leqslant 0.65$ distance to saturation have minimum value. On the other hand, for the range out of $0.45 \leqslant \Delta\gamma \leqslant 0.65$ the distance to saturation increases. As was seen in figure 6 employing an axial GMF does not affect strongly the amplitude of the radiation output. Thus, the difference value of the initial energy of two beams (which corresponds to relativistic factor) that we chose for our simulation is reasonable.

5. Conclusion

Using a self-consistent nonlinear theory, the effect of the GMF on the saturation mechanism in a two-stream FEL model is verified. In this study, the slippage of radiation over the electron bunch is ignored and time plays no role in this 1-D

https://doi.org/10.1017/S0022377815001427 Published online by Cambridge University Press

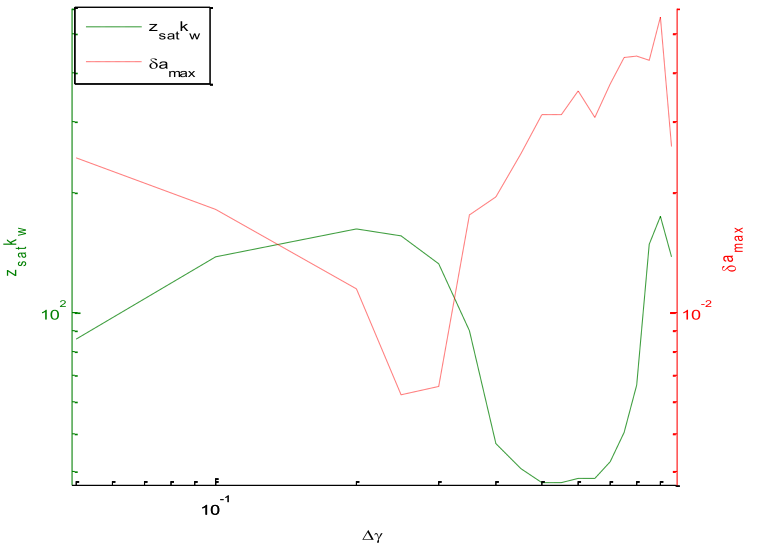


FIGURE 12. Graphs of the maximum amplitude (red) and the distance to the saturation (azure) versus scaled the difference of initial two beams energy.

simulation. By means of scalar potential raising from the current sources the self-field effects of the electron beam have been included. Dependence of the wiggler field amplitude upon the axial position which formed the adiabatic injection of the beam into the interaction region was considered. The effect of the initial adiabatic increase of the wiggler field amplitude on the single particle orbit was verified by numerically solving of electron orbit equations in the absence of electromagnetic and electrostatic fields. In order to improve the efficiency an axial GMF is employed. It is found that for $1.788 \leqslant \hat{\Omega}_0$ large fluctuation in the electron velocity occurs and the electron trajectory exhibits large oscillations about the steady-state orbit, so the injection process did not work well in this range. Employing the GMF as a focusing mechanism for parameters constitute Group II orbit for: $\hat{\Omega}_0 = 1.7$, $\hat{\Omega}_w = 0.4$, $\gamma_1 = 3.5$, $\gamma_2 = 3.0$, $\bar{\omega}_{b1} = 0.4$, $\bar{\omega}_{b2} = 0.42$ and $\omega/ck_w = 5.837$ cause a decrease in the saturation distance to approximately 37.94 %. However, it did not have a strong effect on the amplitude of the radiation. For parameters consistent to the Group I orbit using GMF did not affect strongly the saturation length as well as amplitude of the radiation. This result is reasonable because Group II orbits require an electron beam with higher energy compared to the Group I orbits, hence, they experience a stronger GMF. In fact, increases in the GMF correspond to increases in the resonant frequency and cause a decrease in the divergence from the steady-state trajectories. It was shown that using GMF which is usually used for the focusing purpose can also be considered as a tuning parameter for adjusting the wavelength of the output radiation of the two-stream FELs even with fixed wiggler period and beam energies.

Appendix A. Derivation of dynamical equation

Here, derivation of (3.6) for the evolution of radiation is presented. In the Coulomb gauge, the Maxwell equations can be written as (Freund & Antonsen 1996)

$$\left(\frac{\partial^2}{\partial \bar{z}^2} - \frac{\partial^2}{\partial \bar{t}^2}\right) \delta \boldsymbol{a}(\bar{z}, \bar{t}) = -4\pi \delta \boldsymbol{J}_\perp(\bar{z}, \bar{t}) \tag{A 1}$$

https://doi.org/10.1017/S0022377815001427 Published online by Cambridge University Press

and

$$\left(\frac{\partial^2}{\partial\bar{z}\partial\bar{t}}\right)\delta\varphi(\bar{z},\bar{t}) = 4\pi\delta J_z(\bar{z},\bar{t}), \tag{A 2}$$

where $\delta J_\perp(\bar{z},\bar{t})$ and $\delta J_z(\bar{z},\bar{t})$ are the transverse and the longitudinal (z direction) component of the nonlinear current density, respectively. The current density can be written as an average over the entry time $\bar{t}_0$ (defined as the time at which an electron crosses the $\bar{z}=0$ plane) (Freund 1983; Freund & Antonsen 1996)

$$\delta\boldsymbol{J}(\bar{z},\bar{t}) = -\sum_{i=1}^{2}\frac{\omega_{bi}^2}{4}\int_{-\infty}^{+\infty}\mathrm{d}\bar{t}_0\,\sigma(\bar{t}_0)\boldsymbol{\beta}_i(\bar{t},\bar{t}_0)\frac{\delta[\bar{t}-\tau_i(\bar{z},\bar{t}_0)]}{|\beta_{zi}(\bar{t},\bar{t}_0)|}, \tag{A 3}$$

where $\boldsymbol{\beta}_i(\bar{t},\bar{t}_0)$ is the scaled velocity at time of an electron which crossed the entry plan at time, $\sigma(\bar{t}_0)$ is the distribution in entry time, and

$$\tau_i(\bar{z},\bar{t}_0) = \bar{t}_0 + \int_0^{\bar{z}}\frac{\mathrm{d}\bar{z}'}{\beta_{zi}(\bar{z}',\bar{t}_0)} \tag{A 4}$$

is a Lagrangian time coordinate which measures the time at which an electron reaches the axial position z.

Substituting (3.1) into the Maxwell equations, we have

$$-4\pi\delta J_x = \left(\frac{\mathrm{d}^2}{\mathrm{d}\bar{z}^2}+\bar{\omega}^2-\bar{k}_+^2\right)\delta a\cos\alpha_+ - 2\sqrt{\bar{k}_+}\frac{\mathrm{d}}{\mathrm{d}z}\left(\sqrt{\bar{k}_+}\delta a\right)\sin\alpha_+, \tag{A 5}$$

and

$$4\pi\delta J_y = \left(\frac{\mathrm{d}^2}{\mathrm{d}\bar{z}^2}+\bar{\omega}^2-\bar{k}_+^2\right)\delta a\sin\alpha_+ + 2\sqrt{\bar{k}_+}\frac{\mathrm{d}}{\mathrm{d}z}\left(\sqrt{\bar{k}_+}\delta a\right)\cos\alpha_+. \tag{A 6}$$

Multiply (A 5) by $\cos\alpha_+$, (A 6) by $\sin\alpha_+$, average over wave period; add the resultent equations and substitute of the source currents to obtain

$$\begin{aligned}\left(\frac{\mathrm{d}^2}{\mathrm{d}\bar{z}^2}+\bar{\omega}^2-\bar{k}_+^2\right)\delta a \;=\; &\sum_{i=1}^{2}\omega_{bi}^2\beta_{z0i}\frac{\omega}{2\pi}\int_{-\pi/\omega}^{\pi/\omega}\mathrm{d}t\int_{-\infty}^{+\infty}\mathrm{d}\bar{t}_0\,\sigma(\bar{t}_0)\\ &\times\frac{\delta[t-\tau_i(\bar{z},\bar{t}_0)]}{|\beta_{zi}(\bar{z},\bar{t}_0)|}(v_{xi}\cos\alpha_+ - v_{yi}\sin\alpha_+)\end{aligned} \tag{A 7}$$

and

$$\begin{aligned}2\sqrt{\bar{k}_+}\frac{\mathrm{d}}{\mathrm{d}\bar{z}}\left(\sqrt{\bar{k}_+}\delta a\right) \;=\; &-\sum_{i=1}^{2}\omega_{bi}^2\beta_{z0i}\frac{\omega}{2\pi}\int_{-\pi/\omega}^{\pi/\omega}\mathrm{d}t\int_{-\infty}^{+\infty}\mathrm{d}\bar{t}_0\,\sigma(\bar{t}_0)\\ &\times\frac{\delta[\bar{t}-\tau_i(\bar{z},\bar{t}_0)]}{|\beta_{zi}(\bar{z},\bar{t}_0)|}(v_{xi}\sin\alpha_+ + v_{yi}\cos\alpha_+).\end{aligned} \tag{A 8}$$

For a steady-state amplifier model, the fluctuating fields do not vary in time, but vary in axial position. In this model, two electrons in the interaction region which separated in time by integral multiples of the wave period execute identical trajectories. So, there is no necessity of filling the entire interaction region with electrons, with consideration

https://doi.org/10.1017/S0022377815001427 Published online by Cambridge University Press

of only one beamlet of electron which enters the interaction region during a wave period (Freund & Antonsen 1996).

Using a rotating frame (i.e. (2.3)) we find that

$$\left(\frac{\mathrm{d}^2}{\mathrm{d}\bar{z}^2}+\bar{\omega}^2-\bar{k}_+^2\right)\delta a=\sum_{i=1}^{2}\omega_{bi}^2\beta_{z0i}\left\langle\frac{u_{1i}\cos\psi_i-u_{2i}\sin\psi_i}{|u_{3i}|}\right\rangle, \tag{A 9}$$

$$2\sqrt{\bar{k}_+}\frac{\mathrm{d}}{\mathrm{d}\bar{z}}\left(\sqrt{\bar{k}_+}\delta a\right)=-\sum_{i=1}^{2}\omega_{bi}^2\beta_{z0i}\left\langle\frac{u_{1i}\sin\psi_i-u_{2i}\cos\psi_i}{|u_{3i}|}\right\rangle. \tag{A 10}$$

Equations (A 9) and (A 10) can be reduced to three first-order differential equations for δa, Γ_+ and $\bar{k}_+$ where Γ_+ defines the growth rate of the vector potential. Using definition of growth rate $\mathrm{d}(\ln\delta a)/\mathrm{d}\bar{z}\equiv\Gamma_+$ and relation

$$\frac{\mathrm{d}^2}{\mathrm{d}\bar{z}^2}\delta a=\frac{\mathrm{d}}{\mathrm{d}\bar{z}}(\Gamma_+\delta a)=\delta a\frac{\mathrm{d}}{\mathrm{d}\bar{z}}\Gamma_++\Gamma_+\frac{\mathrm{d}}{\mathrm{d}\bar{z}}\delta a, \tag{A 11}$$

the dynamical equations take the form of

$$\frac{\mathrm{d}\delta a}{\mathrm{d}\bar{z}}\equiv\Gamma_+\delta a, \tag{A 12}$$

$$\frac{\mathrm{d}\Gamma_+}{\mathrm{d}\bar{z}}=(-\bar{\omega}^2+\bar{k}_+^2-\Gamma_+^2)+\sum_{i=1}^{2}\frac{\omega_{bi}^2}{\delta a}\left\langle\frac{u_{1i}\cos\psi_i-u_{2i}\sin\psi_i}{|u_{3i}|}\right\rangle, \tag{A 13}$$

$$\frac{\mathrm{d}\bar{k}_+}{\mathrm{d}\bar{z}}=-2\bar{k}_+\Gamma_+-\sum_{i=1}^{2}\frac{\omega_{bi}^2\beta_{z0i}}{\delta a}\left\langle\frac{u_{1i}\sin\psi_i+u_{2i}\cos\psi_i}{|u_{3i}|}\right\rangle. \tag{A 14}$$

By an analogous procedure for (A 2) we can find an equation for the evolution of the amplitude and wavenumber of the space-charge potential,

$$\frac{\mathrm{d}\delta\varphi}{\mathrm{d}\bar{z}}=-2\sum_{i=1}^{2}\frac{\omega_{bi}^2\beta_{z0i}}{\bar{\omega}}\langle\sin\psi_{sci}\rangle. \tag{A 15}$$

REFERENCES

AGHAMIR, F. M. & MAHDIZADEH, N. 2012 Effects of beam temperature and density variation on the growth rate of a two-stream free electron laser. *Phys. Plasmas* **19**, 032114.

BEKEFI, G. & JACOBS, K. D. 1982 Two-stream free electron laser. *J. Appl. Phys.* **53**, 4113–4121.

BOTTON, M. & RON, A. 1990 Two-stream instability in free electron lasers. *J. Appl. Phys.* **67** (10), 6583–6586.

FREUND, H. P. 1983 Nonlinear analysis of free-electron-laser amplifiers with axial guide fields. *Phys. Rev.* A **27**, 4.

FREUND, H. P. JR & ANTONSEN, T. M. 1996 *Principles of Free Electron Laser*. p. 162. Chapman & Hall.

KULISH, V. V., LYSENKO, A. V. & SAVECHENKO, V. I. 2003 Two-stream free electron lasers: general properties. *Intl J. Infrared Millimeter Waves* **24**, 129–172.

LIU, W., YANG, Z. & LIANG, Z. 2006 Instability of two-stream free-electron laser with an axial guiding magnetic field. *Int. J. Infrared Millimeter Waves* **27**, 1073–1085.

https://doi.org/10.1017/S0022377815001427 Published online by Cambridge University Press

MAHDIZADEH, N. & AGHAMIR, F. M. 2012 Effect of two-stream instability on the saturation mechanism of a two-stream free electron laser with a helical wiggler pump. *Nucl. Instrum. Meth. Phys. Res.* A **688**, 51–54.

MCNEIL, B. W. J., ROBB, G. R. M. & POOLE, M. W. 2004 Two-beam free-electron laser. *Phys. Rev.* E **70**, 035501(R).

MEHDIAN, H., SAVIZ, S. & HASANBEIGI, A. 2008 Two-stream instability in free electron lasers with a planar wiggler and an axial guide magnetic field. *Phys. Plasmas* **15**, 043103.

MIRIAN, N. S. & MARAGHECHI, B. 2013 Thermal effect on prebunched two-beam free electron laser. *Phys. Plasmas* **20**, 083102.

RAGHAVI, A., DE NINNO, G. & MEHDIAN, H. 2008 Effects of ion-channel guiding on the saturation of a single-pass free-electron laser. *Nucl. Instrum. Meth. Phys. Res.* A **591**, 338.

ROBERSON, C. W. & SPRANGLE, P. 1989 A review of free-electron lasers. *Phys. Fluids* B **1**, 3.

ROUHANI, M. H & MARAGHECHI, B. 2010 Three-dimensional simulation of harmonic up-conversion in a prebunched two-beam free-electron laser. *Phys. Rev. Special Topics - Accelerators Beams* **13**, 080706.

ROUHANI, M. H., MARAGHECHI, B. & SABERI, H. 2009 Efficiency enhancement of a two-beam free-electron laser. *Phys. Plasmas* **16**, 123105.

SPRANGLE, P., TANG, C.-M. & MANHEIMER, W. M. 1980 Nonlinear theory of free-electron lasers and efficiency enhancement. *Phys. Rev.* A **21**, 1.

https://doi.org/10.1017/S0022377815001427 Published online by Cambridge University Press